A Deterministic Model Predicts the Properties of Stochastic Calcium Oscillations in Airway Smooth Muscle Cells

Pengxing Cao[1], Xiahui Tan[2], Graham Donovan[1], Michael J. Sanderson[2], James Sneyd[1]*

1 Department of Mathematics, University of Auckland, Auckland, New Zealand, 2 Department of Microbiology and Physiological Systems, University of Massachusetts Medical School, Worcester, Massachusetts, United States of America

Abstract

The inositol trisphosphate receptor (IP_3R) is one of the most important cellular components responsible for oscillations in the cytoplasmic calcium concentration. Over the past decade, two major questions about the IP_3R have arisen. Firstly, how best should the IP_3R be modeled? In other words, what fundamental properties of the IP_3R allow it to perform its function, and what are their quantitative properties? Secondly, although calcium oscillations are caused by the stochastic opening and closing of small numbers of IP_3R, is it possible for a deterministic model to be a reliable predictor of calcium behavior? Here, we answer these two questions, using airway smooth muscle cells (ASMC) as a specific example. Firstly, we show that periodic calcium waves in ASMC, as well as the statistics of calcium puffs in other cell types, can be quantitatively reproduced by a two-state model of the IP_3R, and thus the behavior of the IP_3R is essentially determined by its modal structure. The structure within each mode is irrelevant for function. Secondly, we show that, although calcium waves in ASMC are generated by a stochastic mechanism, IP_3R stochasticity is not essential for a qualitative prediction of how oscillation frequency depends on model parameters, and thus deterministic IP_3R models demonstrate the same level of predictive capability as do stochastic models. We conclude that, firstly, calcium dynamics can be accurately modeled using simplified IP_3R models, and, secondly, to obtain qualitative predictions of how oscillation frequency depends on parameters it is sufficient to use a deterministic model.

Introduction

Oscillations in cytoplasmic calcium concentration ($[Ca^{2+}]_i$), mediated by inositol trisphosphate receptors (IP_3R; a calcium channel that releases calcium ions (Ca^{2+}) from the endoplasmic or sarcoplasmic reticulum (ER or SR) in the presence of inositol trisphosphate (IP_3)) play an important role in cellular function in many cell types. Hence, a thorough knowledge of the behavior of the IP_3R is a necessary prerequisite for an understanding of intracellular Ca^{2+} oscillations and waves. Mathematical and computational models of the IP_3R play a vital role in studies of Ca^{2+} dynamics. However, over the past decade, two major questions about IP_3R models have arisen.

Firstly, how best should the IP_3R be modeled? Models of the IP_3R have a long history, beginning with the heuristic models of [1–3]. With the recent appearance of single-channel data from IP_3R *in vivo* [4,5], a new generation of Markov IP_3R models has recently appeared [6,7]. These models show that IP_3R exist in different modes with different open probabilities. Within each mode there are multiple states, some open, some closed. Importantly, it was found [8] that time-dependent transitions between different modes

are crucial for reproducing Ca^{2+} puff data from [9]. However, it is not yet clear whether transitions between states within each mode are important, or whether all the important behaviors are captured simply by inter-mode transitions.

Secondly, why do deterministic models of the IP_3R perform so well as predictive models? Deterministic models of the IP_3R have proven to be useful predictive models in a range of cell types. For example, IP_3R-based models have been developed to study Ca^{2+} oscillations in airway smooth muscle cells (ASMC) [10–13], and these models have made predictions which have been confirmed experimentally. This shows the usefulness of such models in advancing our understanding of how intracellular Ca^{2+} oscillations and waves are initiated and controlled in ASMC. However, these models are deterministic models which assume infinitely many IP_3R per unit cell volume, an assumption that contradicts experimental findings in many cell types showing that Ca^{2+} puffs and spikes occur stochastically, and that intracellular Ca^{2+} waves and oscillations arise as an emergent property of fundamental stochastic events [9,14,15].

Here, we answer these two fundamental modeling questions using data and models from ASMC. Firstly, we show that a simple

Author Summary

The inositol trisphosphate receptor (IP_3R) is one of the most important cellular components responsible for calcium oscillations. Over the past decade, two major questions about the IP_3R have arisen. Firstly, what fundamental properties of the IP_3R allow it to perform its function? Secondly, although calcium oscillations are caused by the stochastic properties of small numbers of IP_3R is it possible for a deterministic model to be a reliable predictor of calcium dynamics? Using airway smooth muscle cells as an example, we show that calcium dynamics can be accurately modeled using simplified IP_3R models, and, secondly, that deterministic models are qualitatively accurate predictors of calcium dynamics. These results are important for the study of calcium dynamics in many cell types.

model of the IP_3R, involving only two states with time-dependent transitions, suffices to generate correct dynamics of Ca^{2+} puffs and oscillations. Secondly, we show that, although Ca^{2+} oscillations in ASMC are generated by a stochastic mechanism, a deterministic model can make the same qualitative predictions as the analogous stochastic model, indicating that deterministic models, that require much less computational time and complexity, can be used to make reliable predictions. Although we work in the specific context of ASMC, our results are applicable to other cell types that exhibit similar Ca^{2+} oscillations and waves.

Results

A two-state model of the IP_3R is sufficient to reproduce function

We have previously shown [8] that the statistics of Ca^{2+} puffs in SH-SY5Y cells can be reproduced by a Markov model of the IP_3R based on the steady-state data of [5] and the time-dependent data of [4]. In this model the IP_3R can exist in 6 different states, grouped into two modes, which we call *Drive* and *Park* (see Fig. 1). The Drive mode (which contains 4 states; 1 open and 3 closed) has an average open probability of around 0.7, while the Park mode (which contains the remaining two states; 1 open and 1 closed) has an open probability close to zero. Transitions between states within each mode are independent of Ca^{2+} and IP_3; only the transitions between modes are ligand-dependent.

In our previous study on calcium puffs [8], we showed that, to reproduce the experimentally observed non-exponential interspike interval (ISI) distribution and coefficient of variation (CV) of ISI smaller than 1, the time-dependent intermodal transitions are crucial. Lack of time dependencies in the Siekmann model leads to exponential ISI distributions and CV = 1, which is not the case for calcium spikes in ASMC. Fig. 2A shows an example of Ca^{2+} oscillations generated by 50 nM methacholine (MCh, an agonist that can induce the production of IP_3 by binding to a G protein-coupled receptor in the cell membrane) in ASMC. By gathering data from 14 cells in 5 mouse lung slices, we found that the standard deviation of the interspike interval (ISI) is approximately a linear function of the ISI mean, with a slope clearly between 0 and 1 (i.e. CV < 1), indicating that the spikes are generated by an inhomogeneous Poisson process (a slope of 1 would denote a pure Poisson process) (see Fig. 2B). This shows the necessity of inclusion of time-dependent transitions for mode-switching.

Using a quasi-steady-state approximation, and ignoring states with very low dwell times, it is possible to construct a simplified two-state version of the full six-state model (see *Materials and*
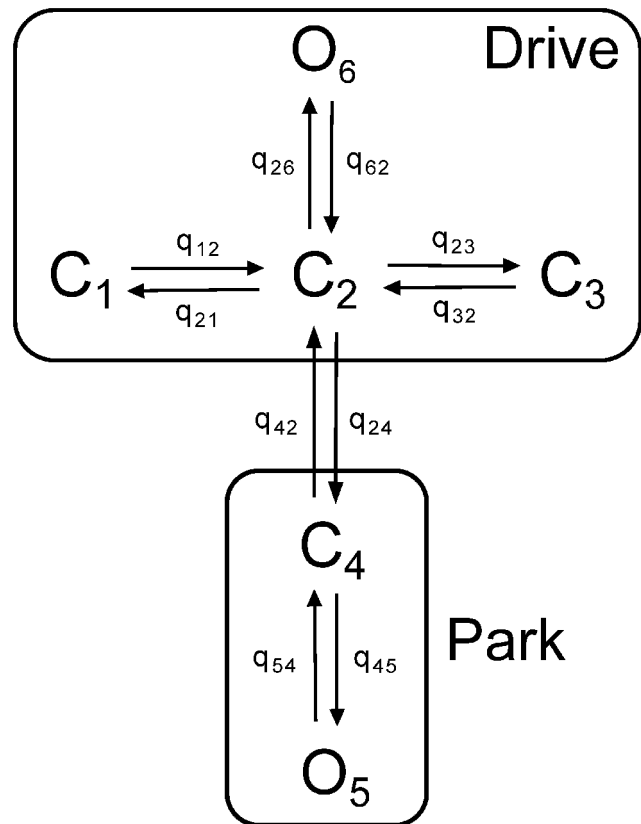

Figure 1. The structure of the Siekmann IP_3R model. The IP_3R model is comprised of two modes. One is the drive mode containing three closed states C_1, C_2, C_3 and one open state O_6. The other is the park mode which includes one closed state C_4 and one open state O_5. qs are rates of state-transitions between two adjacent states and q_{42} and q_{24} are transitions between the two modes [7].
doi:10.1371/journal.pcbi.1003783.g001

Methods). In the simplified model the intramodal structure is ignored, and only the intermodal transitions have an effect on IP_3R behavior. In Fig. 3 we compared the simplified IP_3R model to the full six-state model. Both models have the same distribution of interspike interval, spike amplitude and spike duration. Moreover, by looking at a more detailed comparison between the two model results (Figs. 4A, C and E) and experimental data (Figs. 4B, D and F), we found the 2-state model not only can reproduce the behaviour of the 6-state model, but can also qualitatively reproduce experimental data. The average experimental ISI shows a clear decreasing trend as MCh concentration increases (although a saturation occurs in the data for high MCh), a trend that is mirrored by the model results as the IP_3 concentration increases. Unfortunately, since the exact relationship between MCh concentration and IP_3 concentration is uncertain, a quantitative comparison is not possible. In both model and experimental results, the average peak and duration of the oscillations are nearly independent of agonist concentration. The quantitative difference in spike duration between the model results and the data in Figs. 4E and F are most likely due to choice of calcium buffering parameters. For example, adding 3 or 5 μM fast Ca^{2+} buffer (see *Materials and Methods*) increases the average spike duration to 0.54 s or 0.7 s respectively, which are close to the levels shown in the data.

Thus, the intramodal structure of the six-state model is essentially unimportant, as the model behavior (in terms of the
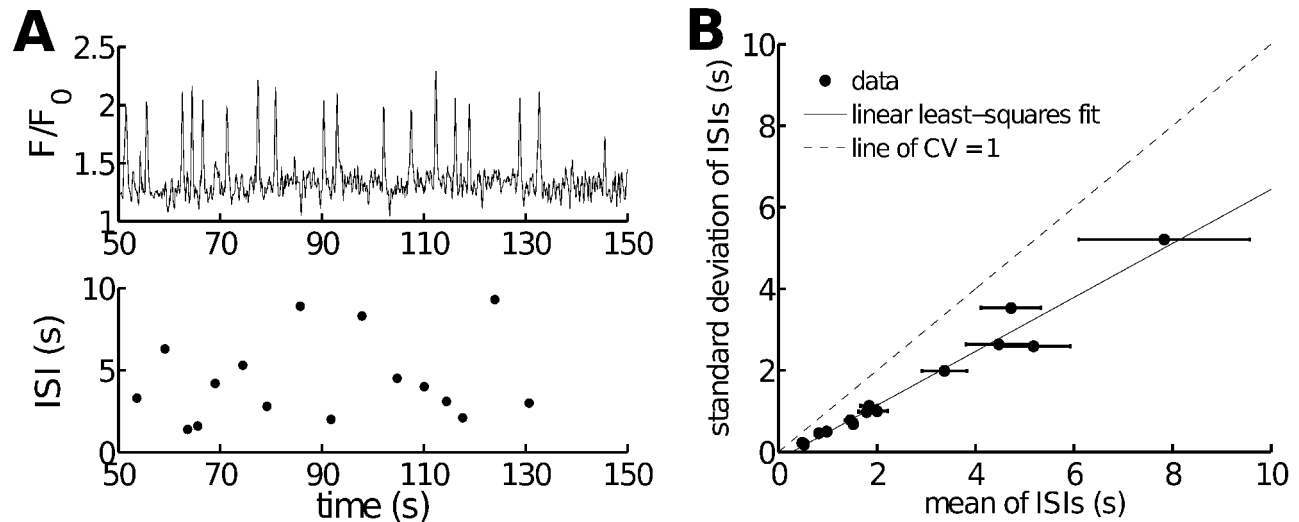
Figure 2. Ca^{2+} oscillations in ASMC in lung slices are generated by a stochastic mechanism. A: experimental Ca^{2+} spiking in ASMC in lung slices, stimulated with 50 nM MCh. In the upper panel we filter out baseline noise by using a low threshold of 1.42 (relative fluorescence intensity) and then choose samples with amplitude larger than 1.75. The ISI calculated from the upper panel is shown in the lower panel. **B**: relationship between the standard deviation and the mean of experimental ISIs. Data obtained from 14 ASMC in 5 mouse lung slices. The relationship is approximately linear with a slope of 0.66, which implies that an inhomogeneous Poisson process governs the generation of oscillations. The dashed line indicates where the coefficient of variation (CV) is 1 (as it is for a pure Poisson process). Variation in ISI is mainly caused by both use of different doses of MCh and different sensitivities of different cells to MCh. Error bars indicate the standard errors of the means (SEM).
doi:10.1371/journal.pcbi.1003783.g002

statistics of puffs and oscillations) is governed almost entirely by the time dependence of the intermode transitions, particularly the time dependence of the rapid inhibition of the IP$_3$R by high [Ca^{2+}]$_i$, and the slow recovery from inhibition by Ca^{2+}. The multiple states within each mode are necessary to obtain an acceptable quantitative fit to single-channel data, but are nevertheless of limited importance for function. Hence, even when simulating microscopic events such as Ca^{2+} puffs it is sufficient to use a simpler, faster, two-state model, rather than a more complex six-

state model. In the following, we will use the 2-state IP$_3$R model to generate all the simulation results.

Prediction of stochastic Ca^{2+} behavior by a deterministic model

Although the data (Fig. 2) show that Ca^{2+} oscillations in ASMC are generated by a stochastic process, not a deterministic one, we wish to know to what extent a deterministic model can be used to make qualitative (and experimentally testable) predictions. Our
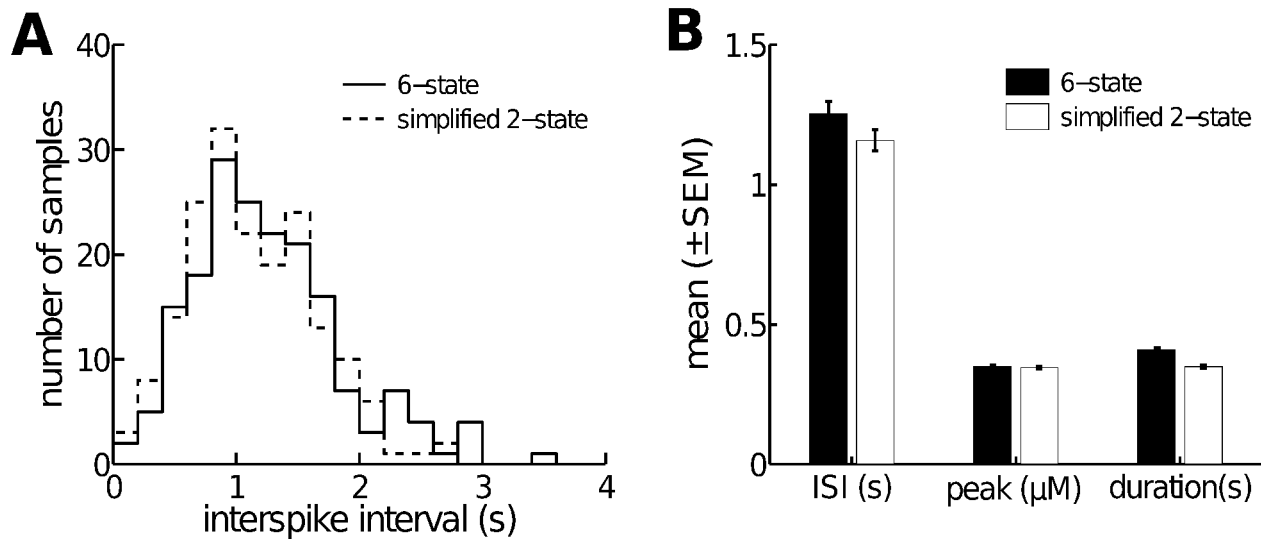
Figure 3. A 2-state open/closed model quantitatively reproduces the 6-state IP$_3$R model. A: histograms of interspike interval (ISI) distribution for both the 6-state and the simplified models. The ISI is defined to be the waiting time between successive spikes. Each histogram contain an equal number of samples (180). **B**: comparison of average ISI, average peak value of [Ca^{2+}]$_i$ (c in the model) and average spike duration. All distributions were computed at a constant [IP$_3$] $= 0.15 \mu$M.
doi:10.1371/journal.pcbi.1003783.g003
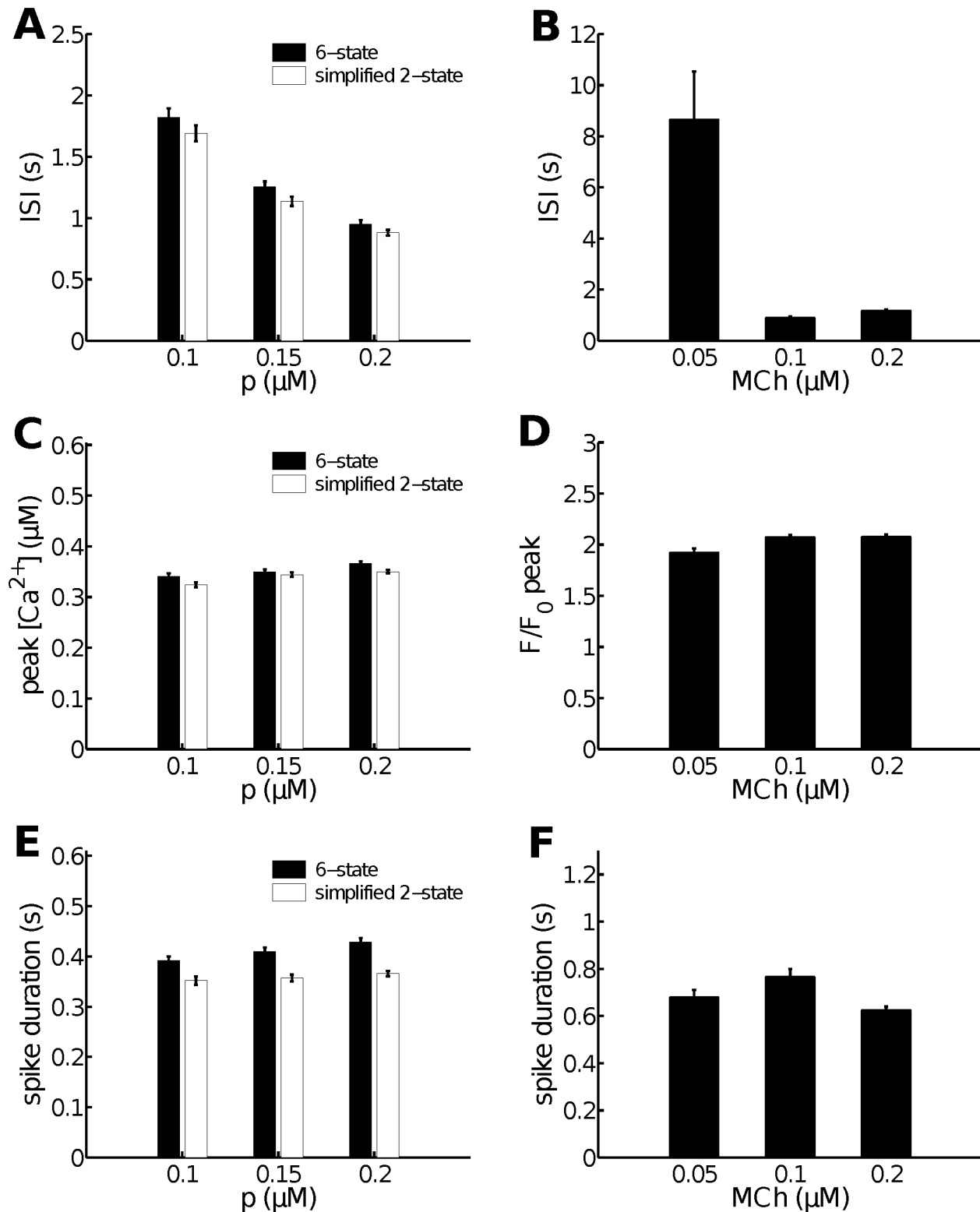
Figure 4. More detailed comparisons between the 2-state and the 6-state IP_3R models, and a comparison to experimental data. As a function of IP_3 concentration (p), the two models give the same ISI (**A**), peak $[Ca^{2+}]_i$ (**C**) and spike duration (**E**). These results agree qualitatively with experimental data, as shown in panels **B**, **D** and **F** respectively. Quantitative comparisons are generally not possible as the relationship between IP_3 concentration and agonist concentration is not known. Error bars represent mean $\pm$ SEM. Data for each MCh concentration are obtained from at least three different cells from at least two different lung slices.

doi:10.1371/journal.pcbi.1003783.g004

simplified 2-state Markov model of the IP_3R can be converted to a deterministic model (see *Materials and Methods*). The result is a system of ordinary differential equations (ODEs) with four variables, which takes into account the increased $[Ca^{2+}]_i$ at an open IP_3R pore, as well as the increased $[Ca^{2+}]_i$ within a cluster of IP_3R; the four variables are the $[Ca^{2+}]_i$ outside the IP_3R cluster (c), the $[Ca^{2+}]_i$ within the IP_3R cluster (c_b), the total intracellular Ca^{2+} concentration (c_t) and an IP_3R gating variable (h_{42}). We refer to the reduced 4D model as the deterministic model for all the results and analyses.

Note that there is no physical or geometric constraint enforcing a high local $[Ca^{2+}]_i$; in this case the spatial heterogeneity arises solely from the low diffusion coefficient of Ca^{2+}. Our use of c_b is merely a highly simplified way of introducing spatial heterogeneity of the Ca^{2+} concentration. Since the IP_3R can only "see" c_b (as well as the Ca^{2+} concentration right at the mouth of an open channel, which we denote by c_p), but cannot be influenced directly by c (the experimentally observed Ca^{2+} signal), our approach allows for the functional differentiation of the rapid local oscillatory Ca^{2+} in the cluster, from the slower Ca^{2+} signal in the cytoplasm, without the need for computationally intensive simulations of a partial differential equation model. Quantitative accuracy is thus sacrificed for computational convenience.

Calcium oscillations in the stochastic and deterministic models are shown in Fig. 5A. According to our previous results [8], the average value of h_{42} over the cluster of IP_3R primarily regulates the termination and regeneration of individual spikes. This can be seen in the stochastic model by projecting the solution on the c_b, h_{42} phase plane (Fig. 5B). Upon an initial Ca^{2+} release from one or more IP_3R, a large spike is generated by Ca^{2+}-induced Ca^{2+} release (via the IP_3R) during which time a decreasing h_{42} gradually decreases the average open probability of the clustered IP_3R. The spike is terminated when h_{42} is too small to allow further Ca^{2+} release. This phenomenon is qualitatively reproduced by the deterministic model (Fig. 5D). In both the stochastic and deterministic models the decrease in average IP_3R open probability of a cluster of IP_3R caused by Ca^{2+} inhibition is the main reason for the termination of each spike.

According to Figs. 5B and D, regeneration of each spike requires a return of h_{42} back to a relatively high value (i.e., recovery of the IP_3R from inhibition by Ca^{2+}). The deterministic model sets a clear threshold for the regeneration, as can be seen in Fig. 5C, where an upstroke in c_b occurs when the trajectory creeps beyond the sharp "knee" of the white curve. When the trajectory reaches the knees of the white curve it is forced to jump across to the other stable branch of the critical manifold, resulting in a fast increase in c_b followed by a relatively fast increase in c (seen by combining Figs. 5C and D).

In contrast, the stochastic model enlarges the contributions of individual IP_3R so that the generation of each spike is also effectively driven by random Ca^{2+} release through the IP_3R, which can be seen in the inset of Fig. 5B where the site of spike initiation (blue bar) exhibits significantly greater variation than that of spike termination (green bar). In spite of this, the essential similarities in phase plane behavior result in both deterministic and stochastic models making the same qualitative predictions in response to perturbations, such as changes in IP_3 concentration ($[IP_3]$), Ca^{2+} influx or efflux. In the following, we illustrate this by investigating a number of experimentally testable predictions. Due to the extensive importance of frequency encoding in many Ca^{2+}-dependent processes, we focus particularly on the change of oscillation frequency in response to parameter perturbations. As a

side issue we also investigate how the oscillation baseline depends on physiologically important parameters.

Dependence of oscillation frequency on IP_3 concentration

In many cell types a moderate increase in $[IP_3]$ increases the Ca^{2+} oscillation frequency (see Fig. 2A in [11], Fig. 4E in [16] and Fig. 6B in [17]), a result that is reproduced by both model types (Fig. 6A). As $[IP_3]$ increases, the stochastic model increases the probability of the initial Ca^{2+} release through the first open IP_3R and of the following Ca^{2+} release, thus shortening the average ISI. Although the oscillatory region of the deterministic model is strictly confined by bifurcations which do not apply to the stochastic model, the deterministic model can successfully replicate an increasing frequency by lowering the "knee" of the red curve in Fig. 5D and shortening the time spent from the termination point c to the initiation point a (thus shortening the ISI). Hence, although the deterministic model cannot be used to predict the exact values of $[IP_3]$ at which the oscillations begin and end, as stochastic effects predominate in these regions, it can be used to predict the correct qualitative trend in oscillation frequency.

Dependence of oscillation frequency on Ca^{2+} influx and efflux

In many cell types, including ASMC, transmembrane fluxes modulate the total intracellular Ca^{2+} load (c_t) on a slow time scale [16,18], and thereby modulate the oscillation frequency [19]. Experimental data can be seen in Fig. 8 in [16] and Fig. 2 in [18]. Figs. 6B and C show that both stochastic and deterministic models predict the same qualitative changes in oscillation frequency in response to changes in membrane fluxes (through membrane ATPase pumps and/or Ca^{2+} influx channels such as receptor-operated channels or store-operated channels).

Dependence of oscillation frequency on SERCA expression

The level of sarco/endoplasmic reticulum calcium ATPase (SERCA) expression (or capacity) is important for airway remodeling in asthma [20] and ASMC Ca^{2+} oscillations [21]. We thus investigated the predictions of the two models in response to changes in SERCA expression (V_s). As V_s decreases, the deterministic model exhibits a decreasing frequency, in agreement with experimental data (see Figs. 3 and 4 in [21]). The same trend is seen in the stochastic model with only 20 IP_3R (see Fig. 6D).

Dependence of oscillation frequency on Ca^{2+} buffer concentration

Calcium buffers have been shown to be able to change the ISI and spike duration, which in turn change the oscillation frequency [15,22]. We compared the effects on the two models of varying total buffer concentration (B_t) by adding one buffer with relatively fast kinetics to the models (see *Materials and Methods* for details). In both models the frequency decreases as B_t increases (see Fig. 6E), which is consistent with experimental data (Fig. 2B in [18]). This is not surprising, because increasing B_t can decrease the effective rates of SR Ca^{2+} release and reuptake.

Dependence of oscillation baseline on Ca^{2+} influx and SERCA expression

Sustained elevations of baseline during agonist-induced Ca^{2+} oscillations or transients have been observed experimentally, and are believed to be a result of an increase in Ca^{2+} influx caused by opening of membrane Ca^{2+} channels [13,16]. Furthermore, there
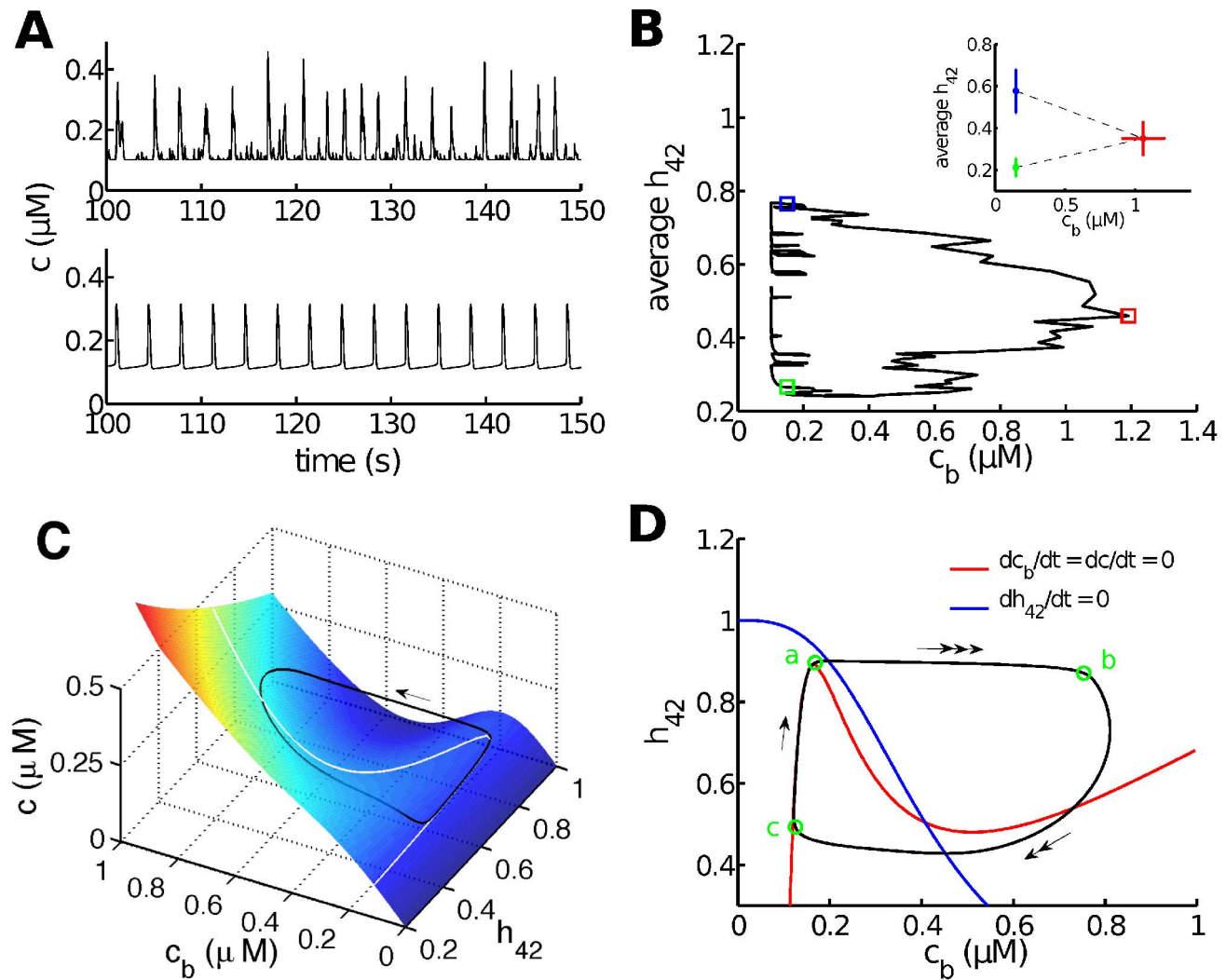
Figure 5. Stochastic and deterministic simulations exhibit similar dynamic properties. A: simulated stochastic (upper panel) or deterministic (lower panel) Ca^{2+} oscillations at 0.1 μM IP_3. **B**: a typical stochastic solution projected on the $c_b - h_{42}$ plane. The average h_{42} represents the average value of h_{42} over the 20 IP_3R. Statistics (mean $\pm$ SD) of the initiation point (blue square), the peak (red square) and termination point (green square) are shown in the inset. 116 samples are obtained by applying a low threshold of 0.15 μM and a high threshold of 0.8 μM to c_b. **C**: a typical periodic solution of the deterministic model (black curve), plotted in the c, c_b, h_{42} phase space. The arrow indicates the direction of movement. c_t is the slowest variable so that its variation during an oscillation is very small. This allows to treat c_t as a constant ($c_t = 53.12$ μM in this case) and study the dynamics of the model in the c, c_b, h_{42} phase space. The color surface is the surface where $dc_b/dt = 0$ (called the critical manifold). The white N-shaped curve is the intersection of the critical manifold and the surface $dc/dt = 0$. **D**: projection of the periodic solution to the c_b, h_{42} plane. The red N-shaped curve is the projection to the c_b, h_{42} plane of the white curve shown in **C**. The evolution of the deterministic solution exhibits three different time scales separated by green circles (labelled by a, b and c) and indicated by arrows (triple arrow: fastest; double arrow: intermediate; single arrow: slowest).
doi:10.1371/journal.pcbi.1003783.g005

is evidence showing that decreased SERCA expression could also increase the baseline (Fig. 4 in [21]). Those phenomena are successfully reproduced by both models (see Fig. 7).

Discussion

In this paper we address two current major questions in the field of Ca^{2+} modeling. Firstly, we show that Ca^{2+} puffs and stochastic oscillations can be reproduced quantitatively by an extremely simple model, consisting only of two states (one open, one closed), with time-dependent transitions between them. This model is obtained by removing the intramodal structure of a more complex model that was determined by fitting a Markov model to single-

channel data [7]. We thus show that the internal structure of each mode is irrelevant for function and mode switching is the key mechanism for the control of calcium release. The necessity for time-dependent mode switching is shown not only by the dynamic single-channel data of [4]), but also by the puff data of [9] and our ASMC data.

Secondly, we investigate the role of stochasticity of IP_3R in modeling Ca^{2+} oscillations in ASMC by comparing a stochastic IP_3R-based Ca^{2+} model and its associated deterministic version, for parameters such that both of the models exhibit Ca^{2+} spikes but the stochastic model cannot necessarily be replaced by a mean-field model. We find that a four-variable deterministic model has the same predictive power as the stochastic model, in
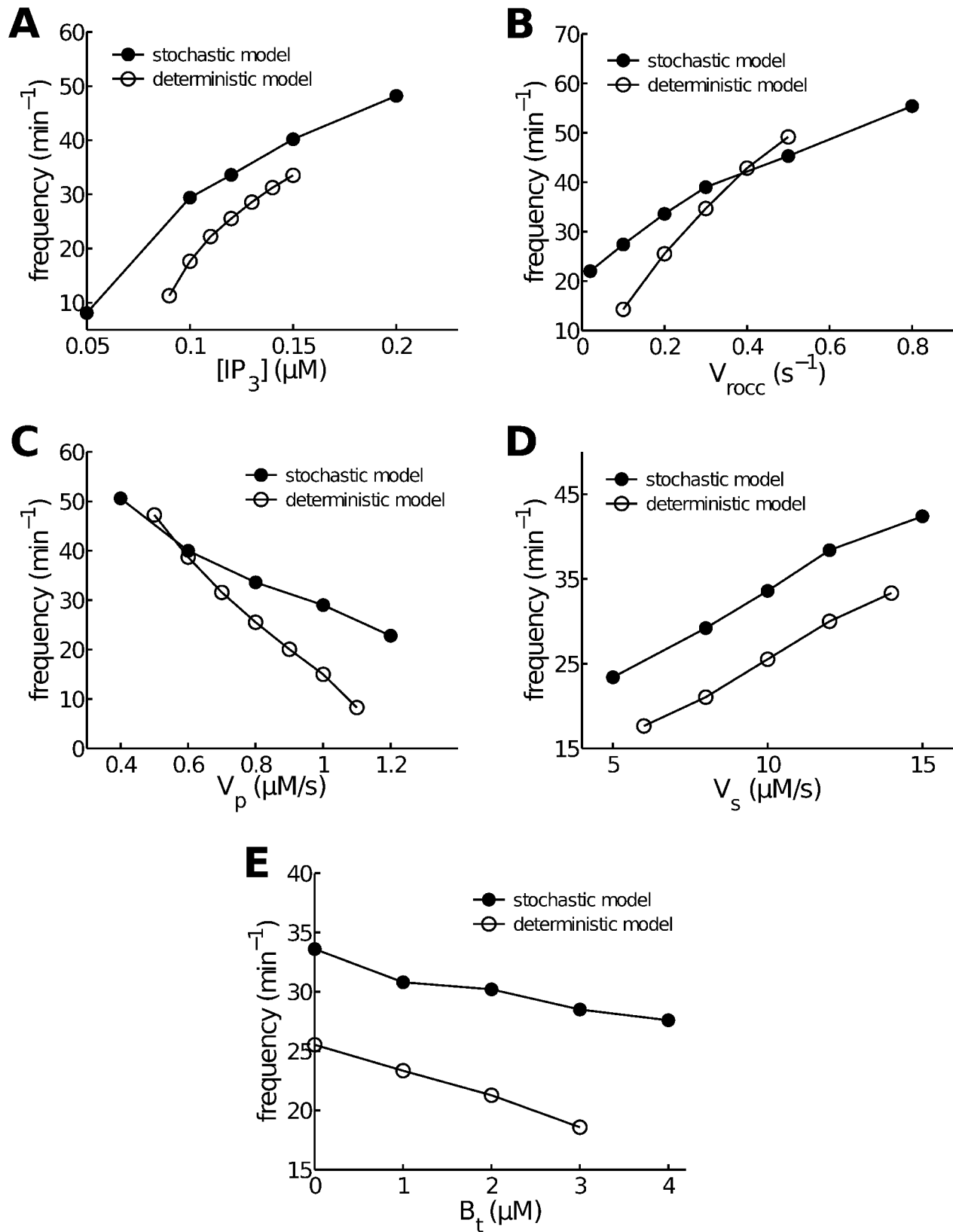
Figure 6. Comparison of parameter-dependent frequency changes in the stochastic and deterministic models. All curves are computed at 0.12 μM IP$_3$ except in panel A, which uses a variety of [IP$_3$]. Other parameters are set at their default values given in Table 1. **A**: as [IP$_3$] increases, Ca^{2+} oscillations in both models increase in frequency. **B**: as Ca^{2+} influx increases (modeled by an increase in receptor-operated calcium channel flux coefficient V_{rocc}), so does the oscillation frequency in both models. **C**: as Ca^{2+} efflux increases (modeled by an increase in plasma pump expression V_p), oscillation frequency decreases. **D**: as SERCA pump expression, V_s, increases, so does oscillation frequency. **E**: as total buffer concentration, B_t, increases, oscillation frequency decreases.
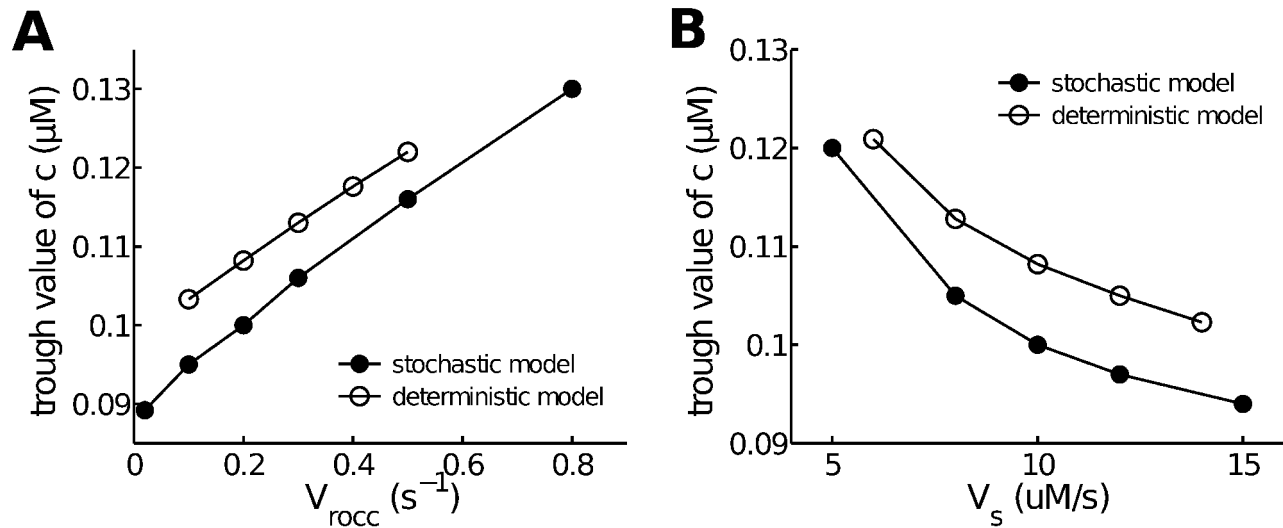doi:10.1371/journal.pcbi.1003783.g006

Figure 7. Dependence of calcium oscillation baseline on calcium influx and SERCA expression. A: increasing influx (described by V_{rocc}) increases the average trough of Ca^{2+} oscillations. **B**: decreasing SERCA expression (described by V_s) increases the average trough of Ca^{2+} oscillations. All curves are computed at $0.12\ \mu M$ IP_3.
doi:10.1371/journal.pcbi.1003783.g007

that it correctly reproduces the process of spike termination and predicts the same qualitative changes in oscillation frequency and baseline in response to a variety of perturbations that are commonly used experimentally. The mechanism for termination of individual spikes is fundamentally a deterministic process controlled by a rapid inhibition induced by the high local $[Ca^{2+}]_i$ in the IP_3R cluster, whereas spike initiation is significantly affected by stochastic opening of IP_3R. Hence, repetitive Ca^{2+} cycling is primarily induced by the time-dependent gating variables governing transitions of the IP_3R from one mode to another.

Our simplified two-state model of the IP_3R is identical in structure (although not in parameter values) to the well-known model of [23]. It is somewhat ironic that after 20 years of detailed studies of the IP_3R and the construction of a plethora of models of varying complexity, the single-channel data have led us around full circle, back to these original formulations. Excitability is arising via a fast activation
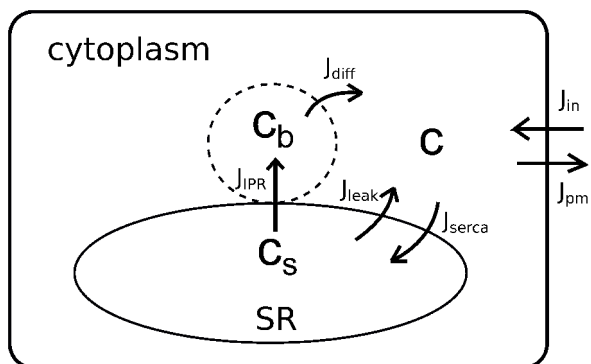
followed by a slower inactivation, a combination often seen in physiological processes [24]. Encoding of this fundamental combination results directly from the two-mode structure of the IP_3R. Although similar single-channel data have been used to construct three-mode models [6,25], neither of these models has yet been used in detailed studies of Ca^{2+} puffs and waves, and it remains unclear whether or not they have a similar underlying structure.

In contrast to previous deterministic ODE models, our four-variable Ca^{2+} model includes a more accurate IP_3R model, as well as local control of clustered IP_3R by two distinct Ca^{2+} microdomains; one at the mouth of an open IP_3R, the other inside a cluster of IP_3R. Neglect of either of these microdomains leads to models that either exhibit unphysiological cytoplasmic Ca^{2+} concentrations or fail to reproduce reasonable oscillations. This underlines the importance of taking Ca^{2+} microdomains into consideration when constructing any model. Our microdomain model is highly simplified, with the microdomain being treated simply as a well-mixed compartment. More detailed modeling of spatially-dependent microdomains is possible, and not difficult in principle, but requires far greater computational resources. It is undeniable that a more detailed model, incorporating the full spatial complexity – and possibly stochastic aspects as well – would make, overall, a better predictive tool. However, our goal is to find the simplest models that can be used as predictive tools.

An important similar study is that of Shuai and Jung [26]. They compared the use of Markov and Langevin approaches to the computation of puff amplitude distributions, compared their results with the deterministic limit, and showed that IP_3R stochasticity does not qualitatively change the type of puff amplitude distribution except for when there are fewer than 10 IP_3R. Here, we significantly extend the scope of their study by exploring the effects of IP_3R stochasticity on the dynamics of Ca^{2+} spikes, and we do this in the context of an IP_3R model that has been fitted to single-channel data. Although this is true in a general sense for the Li-Rinzel model, which is based on the DeYoung-Keizer model, which did take into account the opening time distributions of IP_3R in lipid bilayers, neither model can reproduce the more recent data obtained from on-nuclei patch clamping. When these recent data are taken into account one obtains a model with the same structure, but quite different parameters and behavior.

Figure 8. Schematic diagram of the Ca^{2+} model. c represents cytoplasmic Ca^{2+} concentration, excluding a small local Ca^{2+} (whose concentration is denoted by c_b) close to the Ca^{2+} release site (i.e., an IP_3R cluster). Upon coordinated openings of the IP_3R, SR Ca^{2+} (c_s) is first released into the local domain (J_{IPR}) to cause a rapid increase in c_b. High local Ca^{2+} then diffuses to the rest of the cytoplasm (J_{diff}), and is eventually pumped back to the SR (J_{serca}).
doi:10.1371/journal.pcbi.1003783.g008

Table 1. Parameter values of the stochastic calcium model.

Parameter	Description	Value/Units
k_{IPR}	IP_3R flux coefficient	$0.05\ s^{-1}$
k_{diff}	Ca^{2+} diffusional flux coefficient	$10\ s^{-1}$
k_{leak}	SR leak flux coefficient	$0.0032\ s^{-1}$
V_s	maximum capacity of SERCA	$10\ \mu M \cdot s^{-1}$
K_s	SERCA half-maximal activating $[Ca^{2+}]_i$	$0.26\ \mu M$
n_s	Hill coefficient for SERCA	1.75
J_{leakin}	plasma membrane leak influx	$0.03115\ \mu M \cdot s^{-1}$
V_{rocc}	ROCC flux coefficient	$0.2\ s^{-1}$
V_{socc}	maximum capacity of SOCC	$1.6\ \mu M \cdot s^{-1}$
K_{socc}	SOCC dissociation constant	$100\ \mu M$
V_p	maximum capacity of plasma pump	$0.8\ \mu M \cdot s^{-1}$
K_p	half-maximal activating $[Ca^{2+}]_i$ of plasma pump	$0.5\ \mu M$
n_p	Hill coefficient for plasma pump	2
γ_1	the cytoplasmic-to-microdomain volume ratio	100
γ_2	the cytoplasmic-to-SR volume ratio	10
c_{p0}	an instantaneous high $[Ca^{2+}]_i$ at open channel pore when $c_s = 100\ \mu M$	$120\ \mu M$
N_t	total number of IP_3R channels	20

We find that, in spite of a relatively large variation in spike amplitude which is partially caused by a large variation in ISI (Fig. 5B), the mechanism governing individual spike terminations is the same for both a few or infinitely many IP_3R, which explains why the one-peak type of amplitude distribution is independent of the choice of IP_3R number (see Fig. 6A in [26]).

Another important relevant study was done by Dupont et al. [27], who compared the regularity of stochastic oscillations in hepatocytes for different numbers of IP_3R clusters. They found that the impact of IP_3R stochasticity on global Ca^{2+} oscillations (in terms of CV) increases as the total cluster number decreases. Our study here extends these results, and demonstrates how well stochastic oscillations can be qualitatively described by a deterministic system, even when there is only a small number of IP_3R (which appears to be the case for ASMC, in which the wave initiation site is only $2 \sim 4\ \mu m$ in diameter). Indeed, as we have shown, for the purposes of predictive modeling a simple deterministic model does as well as more complex stochastic simulations.

Ryanodine receptors (RyR) are another important component modulating ASMC Ca^{2+} oscillations [16,28,29] but are not included in our model. This is because the role of RyR is not fully understood and may be species-dependent; for example, in mouse or human ASMC, RyR play very little role in IP_3-induced continuing Ca^{2+} oscillations [17,30], but this appears not to be true for pigs [28]. Our study focuses on the calcium oscillations in mouse and human (as we did in our experiments) where inclusion of a deterministic model of RyR should have little effect. An understanding of the role of RyR stochasticity and how the IP_3R and the RyR interact needs a reliable RyR Markov model, exclusive to ASMC, which is not currently available. Multiple Markov models of the RyR have been developed for use in cardiac cells [31], but these are based on single-channel data from lipid bilayers, and are adapted for the specific context of cardiac cells. Their applicability to ASMC remains unclear.

Although we have not shown that the deterministic model for ASMC has the same predictive power as the stochastic model in all possible cases (which would hardly be possible in the absence of an analytical proof) the underlying similarity in phase plane structure indicates that such similarity is plausible at least. Certainly, we have not found any counterexample to this claim. However, whether or not this claim is true for all cell types is unclear. Some cell types exhibit both local Ca^{2+} puffs and global Ca^{2+} spikes (usually propagating throughout the cells in the form of traveling waves), showing that initiation of such Ca^{2+} spikes requires a synchronization of Ca^{2+} release from more than one cluster of IP_3R [14]. This type of spiking relies on the hierarchical organization of Ca^{2+} signal pathways, in particular the stochastic recruitment of both individual IP_3R and puffs at different levels [32], and therefore cannot be simply reproduced by deterministic models containing only a few ODEs. However, Ca^{2+} oscillations in ASMC, as observed in lung slices, may not be of this type, as IP_3R-dependent puffs have not been seen in these ASMC. It thus appears that, in ASMC in lung slices, every Ca^{2+} "puff" initiates a wave, resulting in periodic waves with ISI that are governed by the dynamics of individual puffs.

Materials and Methods

Ethics Statement

Animal experimentations carried out were approved by the Animal Care and Use Committee of the University of Massachusetts Medical School under approval number A-836-12.

Lung slice preparation

BALB/c mice (7–10 weeks old, Charles River Breeding Labs, Needham, MA) were euthanized via intraperitoneal injection of 0.3 ml sodium pentabarbitone (Oak Pharmaceuticals, Lake Forest,

IL). After removal of the chest wall, lungs were inflated with ~ 1.1 ml of 1.8% warm agarose in sHBSS via an intratracheal catheter. Subsequently, air (~ 0.3 ml) was injected to push the agarose within the airways into the alveoli. The agarose was polymerized by cooling to 4°C. A vibratome (VF-300, Precisionary Instruments, San Jose, CA) was used to make 180 μm thick slices which were maintained in Dulbecco's Modified Eagle's Media (DMEM, Invitrogen, Carlsbad, CA) at 37°C in 10% CO_2/air. All experiments were conducted at 37°C in a custom-made temperature-controlled Plexiglas chamber as described in [17].

Measurement of Ca^{2+} oscillations

Lung slices were incubated in sHBSS containing 20 μM Oregon Green 488 BAPTA-1-AM (Invitrogen), a Ca^{2+}-indicator dye, 0.1% Pluronic F-127 (Invitrogen) and 200 μM sulfobromophthalein (Sigma Aldrich, St Louis, MO) in the dark at 30°C for 1 hour. Subsequently, the slices were incubated in 200 μM sulfobromophthalein for 30 minutes. Slices were mounted on a cover-glass and held down with 200 μm mesh. A smaller cover-glass was placed on top of the mesh and sealed at the sides with silicone grease to facilitate solution exchange. Slices were examined with a custom-built 2-photon scanning laser microscope with a $\times 40$ oil immersion objective lens and images recorded at 30 images per second using Videosavant 4.0 software (IO Industries, Montreal, Canada). Changes in fluorescence intensity (which represent changes in $[Ca^{2+}]_i$) were analyzed in an ASMC of interest by averaging the grey value of a 10×10 pixel region using custom written software. Relative fluorescence intensity (F/F_0) was expressed as a ratio of the fluorescence intensity at a particular time (F) normalized to the initial fluorescence intensity (F_0).

The calcium model

Inhomogeneity of cytoplasmic Ca^{2+} concentration not only exists around individual channel pores of the IP_3R, where a nearly instantaneous high Ca^{2+} concentration at the pore (denoted by c_p) leads to a very sharp concentration profile, but is also seen inside an IP_3R cluster where the average cluster Ca^{2+} concentration (c_b) is apparently higher than that of the surrounding cytoplasm (c) [33]. This indicates that during Ca^{2+} oscillations each IP_3R is controlled by either the pore Ca^{2+} concentration (when it is open) or the cluster Ca^{2+} concentration (when it is closed). Neither of these local concentrations influence cell membrane fluxes or the majority of SERCAs, which we assume to be distributed outside the cluster.

The scale separation between the pore Ca^{2+} concentration and the cluster Ca^{2+} concentration allows to treat c_p as a parameter, providing a simpler way of modeling local Ca^{2+} events (like Ca^{2+} puffs) that has been used in several previous studies [8,34,35]. However, evolution of the cluster concentration and wide-field cytoplasm Ca^{2+} concentration are not always separable, so an additional differential equation for the cluster Ca^{2+} is necessary.

A schematic diagram of the model is shown in Fig. 8. The corresponding ODEs are

$$\frac{dc}{dt} = J_{diff} + J_{leak} - J_{serca} + J_{in} - J_{pm}, \quad (1)$$

$$\frac{dc_b}{dt} = \gamma_1(J_{IPR} - J_{diff}), \quad (2)$$

$$\frac{dc_t}{dt} = J_{in} - J_{pm}, \quad (3)$$

where $c_t = c + c_b/\gamma_1 + c_s/\gamma_2$ representing total intracellular Ca^{2+} concentration, and thus SR Ca^{2+} concentration, c_s is given by $c_s = \gamma_2(c_t - c - c_b/\gamma_1)$. γ_1 and γ_2 are the volume ratios given in Table 1. J_{IPR} is the flux through the IP_3R, J_{leak} is a background Ca^{2+} leak out of the SR, and J_{serca} is the uptake of Ca^{2+} into the SR by SERCA pumps. J_{pm} is the flux through plasma pump, and J_{in} represents a sum of main Ca^{2+} influxes including J_{rocc} (receptor-operated Ca^{2+} channel), J_{socc} (store-operated Ca^{2+} channel) and J_{leakin} (Ca^{2+} leak into the cell). J_{diff} coarsely models the diffusion flux from cluster microdomain to the cytoplasm. Details of the fluxes are

- Different formulations of J_{IPR} give different types of models:

a) For the stochastic model, $J_{IPR} = (k_{IPR}/N_t)N_o(c_s - c)$ where k_{IPR} is the maximum conductance of a cluster of N_t IP_3R (here $N_t = 20$). N_o is the number of open IP_3R determined by the states of IP_3R.

b) For the deterministic model we set $J_{IPR} = k_{IPR}P_o(c_s - c)$ where P_o is the IP_3R open probability, a continuous analogue of N_o/N_t.

To calculate N_o and P_o, we use the IP_3R model of [7,8], with minor modifications described later.

- $J_{diff} = k_{diff}(c_b - c)$.

- $J_{serca} = V_s c^{n_s}/(K_s^{n_s} + c^{n_s})$ where K_s and n_s are obtained from [36].

- $J_{leak} = k_{leak}(c_s - c)$.

- J_{in} includes a basal leak (J_{leakin}), receptor-operated calcium channel (ROCC, J_{rocc}), store-operated calcium channel (SOCC, J_{socc}). By using the IP_3 concentration (p) as a surrogate indicator of MCh concentration, we assume that $J_{rocc} = V_{rocc}p$. SOCC is modeled by $J_{socc} = V_{socc}K_{socc}^4/(K_{socc}^4 + c_s^4)$ [13].

- $J_{pm} = V_p c^{n_p}/(K_p^{n_p} + c^{n_p})$.

Calcium concentration at open channel pore (c_p) does not explicitly appear in the equations but is used in the IP_3R model introduced later. c_p is assumed to be proportional to SR Ca^{2+} concentration (c_s) and is therefore simply modeled by

Table 2. Parameter values of the IP$_3$R model.

Parameter	Value/Units	Parameter	Value/Units
q_{12}	1240 s^{-1}	q_{21}	88 s^{-1}
q_{23}	3 s^{-1}	q_{32}	69 s^{-1}
q_{26}	10500 s^{-1}	q_{62}	4010 s^{-1}
q_{45}	11 s^{-1}	q_{54}	3330 s^{-1}
H	20 s^{-1}	L	0.5 s^{-1}
$\lambda_{m_{24}}$	100 s^{-1}	$\lambda_{m_{42}}$	100 s^{-1}
$\lambda_{h_{24}}$	40 s^{-1}		

doi:10.1371/journal.pcbi.1003783.t002

$c_p = c_{p0}(c_s/100)$ where c_{p0} is the value corresponding to $c_s = 100~\mu M$. Alternatively, c_p can also be assumed to be a large constant (say greater than $100~\mu M$) without fundamentally altering the model dynamics. The choice of c_{p0} is not critical as long as it is sufficiently large to play a role in inactivating the open channels. All the parameter values are given in Table 1.

The data-driven IP$_3$R model

The IP$_3$R model used in our ASMC calcium model is an improved version of the Siekmann IP$_3$R model which is a 6-state Markov model derived by fitting to the stationary single channel data using Markov chain Monte Carlo (MCMC) [5,7,8]. Fig. 1 has shown the structure of the IP$_3$R model which is comprised of two modes; the drive mode, containing three closed states C_1, C_2, C_3 and one open state O_6, and the park mode, containing one closed state C_4 and one open state O_5. The transition rates in each mode are constants (shown in Table 2), but q_{42} and q_{24} which connect the two modes are Ca^{2+}-/IP$_3$-dependent and are formulated as

$$q_{24} = a_{24} + V_{24}(1 - m_{24}h_{24}), \qquad (4)$$

$$q_{42} = a_{42} + V_{42}m_{42}h_{42}, \qquad (5)$$

where m_{24}, h_{24}, m_{42} and h_{42} are Ca^{2+}-/IP$_3$-modulated gating variables. a_{24}, a_{42}, V_{24} and V_{42} are either functions of p or constants and are given later. We assume the gating variables obey the following differential equation,

$$\frac{dG}{dt} = \lambda_G(G_\infty - G), \quad (G = m_{24}, h_{24}, m_{42}, h_{42}), \qquad (6)$$

where G_∞ is the equilibrium and λ_G is the rate at which the equilibrium is approached. Those equilibria are functions of Ca^{2+} concentration at the cytoplasmic side of the IP$_3$R, denoted by $\hat{c}$ in the equations, equal to either c_p or c_b depending on the state of the channel). They are assumed to be

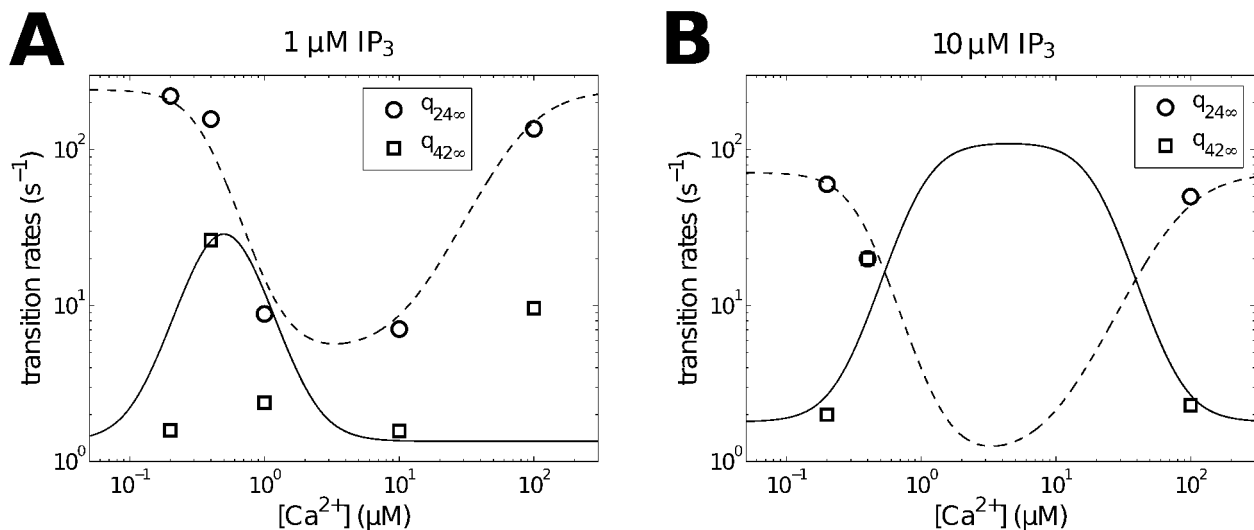$$m_{24\infty} = \frac{\hat{c}^3}{\hat{c}^3 + k_{24}^3}, \qquad (7)$$

Figure 9. Stationary data and fits of q_{24} and q_{42}. Stationary transition rates of q_{24} and q_{42}, $q_{24\infty}$ and $q_{42\infty}$, as functions of Ca^{2+} concentration were estimated and fitted for two [IP$_3$], $1~\mu M$ (**A**) and $10~\mu M$ (**B**). Circles and squares represent the means of q_{24} and q_{42} distributions computed by MCMC simulation [7]. Note that MCMC failed to determine the values of q_{24} and q_{42} at $\hat{c} = 1$, $10~\mu M$ for $10~\mu M$ IP$_3$, as the IP$_3$R was almost in the drive mode for these cases. The corresponding fitting curves (solid for q_{42}; dashed for q_{24}) are produced using Eqs. 7–12.
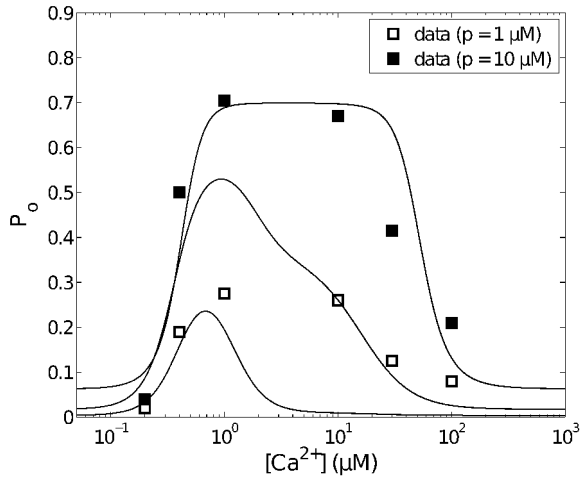doi:10.1371/journal.pcbi.1003783.g009

Figure 10. Open probability curves for various [IP₃]. P_o is equal to the sum of probabilities of the IP$_3$R in O_5 and O_6. Three representative curves correspond to 0.1 μM, 1 μM and 10 μM [IP$_3$] (from bottom to top) respectively. Data (average open probability) are from [5].
doi:10.1371/journal.pcbi.1003783.g010

$$h_{24\infty} = \frac{k_{-24}^2}{\hat{c}^2 + k_{-24}^2}, \tag{8}$$

$$m_{42\infty} = \frac{\hat{c}^3}{\hat{c}^3 + k_{42}^3}, \tag{9}$$

$$h_{42\infty} = \frac{k_{-42}^3}{\hat{c}^3 + k_{-42}^3}. \tag{10}$$

Hence, we have stationary expressions of q_{42} and q_{24},

$$q_{24\infty} = a_{24} + V_{24}(1 - m_{24\infty}h_{24\infty}), \tag{11}$$

$$q_{42\infty} = a_{42} + V_{42}m_{42\infty}h_{42\infty}. \tag{12}$$

The expressions of as, Vs, ns and ks are chosen as follows so that Eq. 11 and Eq. 12 capture the correct trends of experimental values of q_{24} and q_{42} (see Fig. 9) and generate relatively smooth open probability curves (see Fig. 10),

$$
\begin{array}{ll}
V_{24} = 62 + 880/(p^2 + 4) & a_{24} = 1 + 5/(p^2 + 0.25) \\
V_{42} = 110p^2/(p^2 + 0.01) & a_{42} = 1.8p^2/(p^2 + 0.34) \\
k_{24} = 0.35 & k_{42} = 0.49 + 0.543p^3/(p^3 + 64) \\
k_{-24} = 80 & k_{-42} = 0.41 + 25p^3/(p^3 + 274.6)
\end{array}
$$

Note that the above formulas are different from the relatively complicated formulas used in [8]. The rates, $\lambda_{m_{24}}$, $\lambda_{h_{24}}$ and $\lambda_{m_{42}}$, are constants estimated by using dynamic single channel data [4] and

given in Table 2, whereas $\lambda_{h_{42}}$ is not clearly revealed by experimental data. However we have shown that it should be relatively large for high $\hat{c}$ but relatively small for low $\hat{c}$ for reproducing experimental puff data [8]. By introducing two Ca^{2+} concentrations, c_b and c_p, $\lambda_{h_{42}}$ and the state of the IP$_3$R channel become highly correlated, so that we can assume $\lambda_{h_{42}}$ is a relatively large value H if the channel is open and is a relatively small value L if the channel is closed. Hence, $\lambda_{h_{42}}$ is modeled by the logic function

$$\lambda_{h_{42}} = \begin{cases} H, & \text{if the channel is open}; \\ L, & \text{if the channel is closed}. \end{cases}$$

Values of L and H are chosen so that simulated Ca^{2+} oscillations in ASMC are comparable to experimental observations.

The IP$_3$R model reduction

Here we reduce the 6-state model to a 2-state open/closed model. The reduction takes the following steps:

- The sum of the probabilities of C_1, C_3 and O_5 is less than 0.03 for any $\hat{c}$, so they are either rarely visited by the IP$_3$R or have a very short dwell time. This implies they have very little contribution to the Ca^{2+} dynamics. Therefore, we completely remove the three states from the full model.

- Transition rates of q_{26} and q_{62} are about 2 orders larger than that of q_{24} and q_{42}, which allows us to omit the fast transitions by taking a quasi-steady state approximation. This change will affect two aspects. First, we have $O_6 = C_2 q_{26}/q_{62}$ which allows us to combine C_2 and O_6 to be a new state D, which satisfies $D = O_6(q_{62} + q_{26})/q_{26}$. Although this means D is a partially open state with an open probability of $q_{26}/(q_{62} + q_{26})$, it can be used as an fully open state in the stochastic simulations by multiplying the maximum IP$_3$R flux conductance k_{IPR} by a factor of $q_{26}/(q_{62} + q_{26})$. Secondly, q_{24} needs to be rescaled by $q_{62}/(q_{62} + q_{26})$, i.e., the effective closing rate is $q_{24}q_{62}/(q_{62} + q_{26})$.

- Due to the combination of C_2 and O_6, λ_h is accordingly modified to

$$\lambda_{h_{42}} = \begin{cases} H, & \text{if the channel is in } C_4 \\ L, & \text{if the channel is in } D \text{ (the drive mode)} \end{cases}$$

Hence, the reduced two-state model contains one "open" state D and one closed state C_4 with the opening transition rate of q_{42} and the closing transition rate of $q_{24}q_{62}/(q_{62} + q_{26})$.

Deterministic formulation of the stochastic model

Based on the stochastic calcium model and the reduced 2-state IP$_3$R model, we construct a deterministic model. We need to modify three things that are used in the stochastic model but inapplicable to fast simulations of the deterministic model. The first is the discrete number of open channels; the second is state-dependent use of c_b and c_p in calculating q_{42} and q_{24}; the last is the logic expression of $\lambda_{h_{42}}$. Details of the modifications are as follows,

- The fraction of open channels (N_o/N_t) is replaced by open probability P_o which is 70% of the probability of state D.

- In the stochastic simulations, q_{24} which only controls the IP$_3$R closing is primarily governed by c_p, whereas q_{42} which controls IP$_3$R opening is mainly governed by c_b. Therefore, in the deterministic model, we separate the functions of c_p and c_b by assuming $m_{24\infty}$ and $h_{24\infty}$ are functions of c_p only whereas $m_{42\infty}$ and $h_{42\infty}$ are functions of c_b only. That is, $m_{24\infty} = m_{24\infty}(c_p)$, $h_{24\infty} = h_{24\infty}(c_p)$, $m_{42\infty} = m_{42\infty}(c_b)$ and $h_{42\infty} = h_{42\infty}(c_b)$. Here $c_p = c_{p0}(c_s/100)$ as defined before.

- To describe an average rate that infinitely many receptors are rapidly inhibited by high Ca^{2+} concentration but slowly restored from Ca^{2+}-inhibition, $\lambda_{h_{42}}$ is proposed to be

$$\lambda_{h_{42}} = (1-D)L + DH.$$

Based on the above changes, the full deterministic model containing 8 ODEs is presented as follows,

$$\frac{dc}{dt} = J_{\text{diff}} + J_{\text{leak}} - J_{\text{serca}} + J_{\text{in}} - J_{\text{pm}}, \tag{13}$$

$$\frac{dc_b}{dt} = \gamma_1(J_{\text{IPR}} - J_{\text{diff}}), \tag{14}$$

$$\frac{dc_t}{dt} = J_{\text{in}} - J_{\text{pm}}, \tag{15}$$

$$\frac{dD}{dt} = q_{42}(1-D) - \left(\frac{q_{24}q_{62}}{q_{62}+q_{26}}\right)D, \tag{16}$$

$$\frac{dm_{24}}{dt} = \lambda_{m_{24}}\left(\frac{c_p^3}{c_p^3+k_{24}^3} - m_{24}\right), \tag{17}$$

$$\frac{dh_{24}}{dt} = \lambda_{h_{24}}\left(\frac{k_{-24}^2}{c_p^2+k_{-24}^2} - m_{24}\right), \tag{18}$$

$$\frac{dm_{42}}{dt} = \lambda_{m_{42}}\left(\frac{c_b^3}{c_b^3+k_{42}^3} - m_{42}\right), \tag{19}$$

$$\frac{dh_{42}}{dt} = \lambda_{h_{42}}\left(\frac{k_{-42}^3}{c_b^3+k_{-42}^3} - h_{42}\right), \tag{20}$$

where q_{24} and q_{42} are functions of the gating variables given by Eqs. 4 and 5. All the fluxes are the same as those of the stochastic model except $J_{\text{IPR}} = k_{\text{IPR}}(Dq_{26}/(q_{62}+q_{26}))(c_s-c_b)$. All the parameter values of the deterministic model are the same as those of the stochastic model and are therefore given in Tables 1 and 2.

Reduction of the full deterministic model

The full deterministic model contains 8 variables which make the model difficult to implement and analyze. Thus, we reduce the

full model to a minimal model that still captures the crucial features of the full model. First of all, $\lambda_{m_{42}}$, $\lambda_{m_{24}}$ and $\lambda_{h_{24}}$ are sufficiently large so that we can assume they instantaneously follow their equilibrium functions. Therefore, by taking quasi-steady state approximation to m_{24}, h_{24} and m_{42}, we remove the three time-dependent variables from the full model.

By now, the full model has been reduced to a 5D model,

$$\frac{dc}{dt} = J_{\text{diff}} + J_{\text{leak}} - J_{\text{serca}} + J_{\text{in}} - J_{\text{pm}}, \tag{21}$$

$$\frac{dc_b}{dt} = \gamma_1(J_{\text{IPR}} - J_{\text{diff}}), \tag{22}$$

$$\frac{dc_t}{dt} = J_{\text{in}} - J_{\text{pm}}, \tag{23}$$

$$\frac{dD}{dt} = q_{42}(1-D) - \left(\frac{q_{24}q_{62}}{q_{62}+q_{26}}\right)D, \tag{24}$$

$$\frac{dh_{42}}{dt} = \lambda_{h_{42}}\left(\frac{k_{-42}^3}{c_b^3+k_{-42}^3} - h_{42}\right). \tag{25}$$

Second, the rate of change of D approaching its equilibrium, $\lambda_D = (q_{42}q_{62} + q_{42}q_{26} + q_{24}q_{62})/(q_{62}+q_{26})$ (calculated from Eq. 24), is at least one order larger than those of c, c_t and h_{42}, indicating that taking the quasi-steady state approximation to Eq. 24 could not significantly affect the evolutions of c, c_t and h_{42}. That is,

$$D = \frac{q_{42}(q_{62}+q_{26})}{q_{42}q_{62} + q_{42}q_{26} + q_{24}q_{62}}. \tag{26}$$

We emphasize here that the theory of the quasi-steady state approximation has not yet been well established, particularly about the rigorous conditions under which such a reduction is valid. Thus, our criterion of judging the validity of the reduction is checking whether the solutions of the reduced model are capable of qualitatively reproducing that of its original model. For this model, we find the reduction works. Hence, the full model is eventually reduced to a 4D model summarized as follows,

$$\frac{dc}{dt} = J_{\text{diff}} + J_{\text{leak}} - J_{\text{serca}} + J_{\text{in}} - J_{\text{pm}}, \tag{27}$$

$$\frac{dc_b}{dt} = \gamma_1(J_{\text{IPR}} - J_{\text{diff}}), \tag{28}$$

$$\frac{dc_t}{dt} = J_{\text{in}} - J_{\text{pm}}, \tag{29}$$

$$\frac{dh_{42}}{dt} = \lambda_{h_{42}}\left(\frac{k_{-42}^3}{c_b^3+k_{-42}^3} - h_{42}\right), \tag{30}$$

where D is given by Eq. 26.

Inclusion of calcium buffers

To check the effect of calcium buffers on oscillation frequency, we introduce a stationary buffer (no buffer diffusion), as mobile buffers are too complicated to be included in the current deterministic model. Since we have two different cytoplasmic Ca^{2+} concentrations, c and c_b, two pools of buffer with the same kinetics should be considered. Hence, the inclusion of a stationary calcium buffer is modeled by the following system,

$$\frac{dc}{dt} = J_{diff} + J_{leak} - J_{serca} + J_{in} - J_{pm} - k_+(B_t - b_1)c + k_- b_1, \quad (31)$$

$$\frac{dc_b}{dt} = \gamma_1(J_{IPR} - J_{diff}) - k_+(B_t - b_2)c_b + k_- b_2, \quad (32)$$

$$\frac{dc_t}{dt} = J_{in} - J_{pm}, \quad (33)$$

$$\frac{db_1}{dt} = k_+(B_t - b_1)c - k_- b_1, \quad (34)$$

$$\frac{db_2}{dt} = k_+(B_t - b_2)c_b - k_- b_2, \quad (35)$$

where b (b_1 and b_2) and B_t represent the concentrations of Ca^{2+}-bound buffer and total buffer respectively. k_+ and k_- are the rates of Ca^{2+}-binding and Ca^{2+}-dissociation, indicating how fast the time scale of the buffer dynamics is. Fast buffer refers to the buffer with relatively large k_+. In the simulations, we use a fast buffer with $k_+ = 100$ $\mu M^{-1} \cdot s^{-1}$ and $k_- = 100$ s^{-1} and vary B_t to test if the stochastic model and the deterministic model have a qualitatively similar B_t-dependency. Results are given in Fig. 6E.

Numerical methods and tools for deterministic and stochastic simulations

For the stochastic model, Eqs. 1–3 and ODEs of the four gating variables in the IP_3R model are solved by the fourth-order Runge-Kutta method (RK4) and the stochastic states of IP_3R determined by the IP_3R model are solved by using a hybrid Gillespie method with adaptive timing [37]. The maximum time step size is set to be either 10^{-4} s (for the 6-state IP_3R model) or 10^{-3} s (for the reduced 2-state IP_3R model). All the computations are done with MATLAB (The MathWorks, Natick, MA) and the codes are provided in Supporting information (Text S1–S2). For the deterministic model, we use ode15s, an ODE solver in MATLAB. Accuracy is controlled by setting an absolute tolerance of 10^{-8} applied to all the variables.

Statistical analysis

Data analysis is performed on the Ca^{2+} traces with relatively stable baselines and less noise. A moving average of every 3 data points is used to improve the data by smoothing out short-term fluctuations (Fig. 2A is an improved result). Due to large variations in baseline, amplitude, and level of noise in data, we used two thresholds to get samples: a low threshold, 20% of the amplitude of the largest spike above the baseline, to initially filter baseline noise out; and a relatively high threshold, 50% of the amplitude of the largest spike above the baseline, to further remove small spikes that cannot initiate waves. For simulated stochastic traces of variable c, we first convert it to fluorescence ratio (F/F_0) by using $F/F_0 = c(c_0 + K_d)/(c_0 c + c_0 K_d)$ where the dissociation constant of Oregon Green $K_d = 0.17$ μM and resting $[Ca^{2+}]_i$ $c_0 = 0.1$ μM. We then used the same sampling procedure mentioned above to obtain samples. After samples are chosen, ISIs and spike durations are calculated based on the low threshold. Simulated traces used to calculate average frequency are about 200–400 seconds long. All the samplings and linear least-squares fittings are implemented using MATLAB (see Text S3–S4 for Matlab codes).

Supporting Information

Dataset S1 ASMC calcium fluorescence trace data. The data files are in Excel format and compressed in a zip file. Each Excel file has a name showing their information. For example, "S2_SMC6_MCh200nM" means data are from ASMC No. 6 in lung slice No. 2 by using 200 nM MCh. In each file, there are four columns which represent (from left to right) time(s), fluorescence intensity, F/F_0 and average F/F_0.
(ZIP)

Text S1 Matlab code for simulation using 6 state IP_3R model.
(DOCX)

Text S2 Matlab code for simulation using 2 state IP_3R model.
(DOCX)

Text S3 Matlab code for experimental data analysis.
(DOCX)

Text S4 Matlab code for simulation analysis.
(DOCX)

Author Contributions

Conceived and designed the experiments: JS GD MJS. Performed the experiments: XT. Analyzed the data: PC. Contributed to the writing of the manuscript: PC JS. Conceived and designed the model: PC JS GD. Performed the simulations: PC.

References

1. De Young GW, Keizer J (1992) A single-pool inositol 1, 4, 5-trisphosphate-receptor-based model for agonist-stimulated oscillations in Ca^{2+} concentration. Proc Natl Acad Sci USA 89: 9895–9899.
2. Dupont G, Goldbeter A (1993) One-pool model for Ca^{2+} oscillations involving Ca^{2+} and inositol 1,4,5-trisphosphate as co-agonists for Ca^{2+} release. Cell Calcium 14: 311–322.
3. Atri A, Amundson J, Clapham D, Sneyd J (1993) A single-pool model for intracellular calcium oscillations and waves in the *Xenopus laevis* oocyte. Biophys J 65: 1727–1739.
4. Mak DOD, Pearson JE, Loong KPC, Datta S, Fernández-Mongil M, et al. (2007) Rapid ligand-regulated gating kinetics of single $IP3R$ Ca^{2+} release channels. EMBO Rep 8: 1044–1051.
5. Wagner LE, Yule DI (2012) Differential regulation of the InsP3 receptor type-1 and -2 single channel properties by InsP3, Ca^{2+} and atp. J Physiol 590: 3245–3259.
6. Ullah G, Mak DOD, Pearson JE (2012) A data-driven model of a modal gated ion channel: the inositol 1,4,5-trisphosphate receptor in insect sf9 cells. J Gen Physiol 140: 159–173.
7. Siekmann I, Wagner LE, Yule DI, Crampin EJ, Sneyd J (2012) A kinetic model for IP3R type i and type ii accounting for mode changes. Biophys J 103: 658–668.
8. Cao P, Donovan G, Falcke M, Sneyd J (2013) A stochastic model of calcium puffs based on single-channel data. Biophys J 105: 1133–1142.
9. Smith IF, Parker I (2009) Imaging the quantal substructure of single IP3R channel activity during Ca^{2+} puffs in intact mammalian cells. Proc Natl Acad Sci USA 106: 6404–6409.

10. Brumen M, Fajmut A, Dobovišek A, Roux E (2005) Mathematical modelling of Ca²⁺ oscillations in airway smooth muscle cells. J Biol Phys 31: 515–524.

11. Sneyd J, Tsaneva-Atanasova K, Reznikov V, Bai Y, Sanderson MJ, et al. (2006) A method for determining the dependence of calcium oscillations on inositol trisphosphate oscillations. Proc Natl Acad Sci USA 103: 1675–1680.

12. Wang IY, Bai Y, Sanderson MJ, Sneyd J (2010) A mathematical analysis of agonist- and kcl-induced Ca²⁺ oscillations in mouse airway smooth muscle cells. Biophys J 98: 1170–1181.

13. Croisier H, Tan X, Perez-Zoghbi JF, Sandrson MJ, Sneyd J, et al. (2013) Activation of store-operated calcium entry in airway smooth muscle cells: insight from a mathematical model. PLoS ONE 8(7): e69598 doi:10.1371/journal.pone.0069598.

14. Marchant JS, Parker I (2001) Role of elementary Ca²⁺ puffs in generating repetitive Ca²⁺ oscillations. EMBO J 20: 65–76.

15. Skupin A, Kettenmann H, Winkler U, Wartenberg M, Sauer H, et al. (2008) How does intracellular Ca²⁺ oscillate: by chance or by the clock? Biophys J 94: 2404–2411.

16. Perez JF, Sanderson MJ (2005) The frequency of calcium oscillations induced by 5-ht, ach, and kcl determine the contraction of smooth muscle cells of intrapulmonary bronchioles. J Gen Physiol 125: 535–553.

17. Bai Y, Edelmann M, Sanderson MJ (2009) The contribution of inositol 1,4,5-trisphosphate and ryanodine receptors to agonist-induced Ca²⁺ signaling of airway smooth muscle cells. Am J Physiol Lung Cell Mol Physiol 297: L347–L361.

18. Bird GSJ, Putney JW (2005) Capacitative calcium entry supports calcium oscillations in human embryonic kidney cells. J Physiol 562(3): 697–706.

19. Sneyd J, Tsaneva-Atanasova K, Yule DI, Thompson JL, Shuttleworth TJ (2004) Control of calcium oscillations by membrane fluxes. Proc Natl Acad Sci USA 101: 1392–1396.

20. Mahn K, Hirst SJ, Ying S, Holt MR, Lavender P, et al. (2009) Diminished sarco/endoplasmic reticulum Ca²⁺ atpase (serca) expression contributes to airway remodelling in bronchial asthma. Proc Natl Acad Sci USA 106: 10775–10780.

21. Sathish V, Leblebici F, Kip SN, Thompson MA, Pabelick CM, et al. (2008) Regulation of sarcoplasmic reticulum Ca²⁺ reuptake in porcine airway smooth muscle. Am J Physiol Lung Cell Mol Physiol 294: L787–L796.

22. Zeller S, Rüdiger S, Engel H, Sneyd J, Warnecke G, et al. (2009) Modeling of the modulation by buffers of Ca²⁺ release through clusters of IP₃ receptors. Biophys J 97: 992–1002.

23. Li Y, Rinzel J (1994) Equations for InsP₃ receptor-mediated [Ca²⁺]ᵢ oscillations derived from a detailed kinetic model: a hodgkin-huxley like formalism. J Theor Biol 166: 461–473.

24. Keener J, Sneyd J (2009) Mathematical Physiology, Second Edition. Springer, New York.

25. Ionescu L, White C, Cheung KH, Shuai J, Parker I, et al. (2007) Mode switching is the major mechanism of ligand regulation of InsP₃ receptor calcium release channels. J Gen Physiol 130: 631–645.

26. Shuai JW, Jung P (2002) Stochastic properties of Ca²⁺ release of inositol 1,4,5-trisphosphate receptor clusters. Biophys J 83: 87–97.

27. Dupont G, Abou-Lovergne A, Combettes L (2008) Stochastic aspects of oscillatory Ca²⁺ dynamics in hepatocytes. Biophys J 95: 2193–2202.

28. Kannan MS, Prakash YS, Brenner T, Mickelson JR, Sieck GC (1997) Role of ryanodine receptor channels in Ca²⁺ oscillations of porcine tracheal smooth muscle. Am J Physiol 272: L659–L664.

29. Tazzeo T, Zhang Y, Keshavjee S, Janssen LJ (2008) Ryanodine receptors decant internal Ca²⁺ store in human and bovine airway smooth muscle. Eur Respir J 32: 275–284.

30. Ressmeyer AR, Bai Y, Delmotte P, Uy KF, Thistlethwate P, et al. (2010) Human airway contraction and formoterol-induced relaxation is determined by Ca²⁺ oscillations and Ca²⁺ sensitivity. Am J Respir Cell Mol Biol 43: 179–191.

31. Soeller C, Cannell MB (2004) Analysing cardiac excitation-contraction coupling with mathematical models of local control. Prog Biophys Mol Biol 85: 141–162.

32. Thurley K, Skupin A, Thul R, Falcke M (2012) Fundamental properties of Ca²⁺ signals. Biochim Biophys Acta 1820(8): 1185–1194.

33. Dickinson G, Parker I (2013) Factors determining the recruitment of inositol trisphosphate receptor channels during calcium puffs. Biophys J 105: 2474–2484.

34. Rüdiger S, Shuai JW, Sokolov IM (2010) Law of mass action, detailed balance, and the modeling of calcium puffs. Phys Rev Lett 105(4): 048103 doi:10.1103/PhysRevLett.105.048103.

35. Rüdiger S, Jung P, Shuai J (2012) Termination of Ca²⁺ release for clustered IP₃R channels. PLoS Comput Biol 8(5): e1002485 doi:10.1371/journal.pcbi.1002485.

36. Chandrasekera PC, Kargacim ME, Deans JP, Lytton J (2009) Determination of apparent calcium affinity for endogenously expressed human sarco(endo)plasmic reticulum calcium-atpase isoform serca3. Am J Physiol Cell Physiol 296: C1105–C1114.

37. Rüdiger S, Shuai JW, Huisinga W, Nagaiah C, Warnecke G, et al. (2007) Hybrid stochastic and deterministic simulations of calcium blips. Biophys J 93: 1847–1857.